Advances in Nano Research, *Vol. 19, No. 3 (2025) 285-296*
https://doi.org/10.12989/anr.2025.19.3.285

Mathematical modeling for stability and instability analysis of carbon nanotube enhanced fibers in clothing design

Wei Wu[1], Kui Li*[2] and Murat Yaylacı[3,4]

[1]*College of Fine Arts and Design, University of Jinan, Jinan, 250022, China*
[2]*School of Digital Arts and Communication, Shandong University of Art & Design, Jinan, 250399, China*
[3]*Department of Civil Engineering, Recep Tayyip Erdogan University, 53100, Rize, Turkey*
[4]*Turgut Kıran Maritime Faculty, Recep Tayyip Erdogan University, 53900, Rize, Turkey*

(*Received February 1, 2025, Revised September 4, 2025, Accepted September 5, 2025*)

Abstract. The current work provides a mathematical model to evaluate the stability and instability of carbon nanotube (CNT)-reinforced fibers as they are employed in clothing design. We model the textile thread as a double-clamped beam, which indicates the mechanical behavior of the fiber. The fibers are multi-scale hybrid nanocomposites (MHC) or combinations of multi-scale composite, integrated with CNTs for added strength and elasticity. We apply Halpin–Tsai model characterizations for composite materials so that we can evaluate the effective properties of the composite substance and incorporate interaction between CNTs and the matrix. The deformation of the thread is modeled by developing a quasi-3D hybrid type (q-3DHT) formula using higher order shear deformation theory (HSDT). The higher order shear deformation theory represents shear deformation and rotational inertia and provides a more accurate representation of the behavior of the material system. A variational method to derive the governing equations of motion for the system exposed to a harmonically induced transverse force is used in the approach. Following this, the stability of the system is assessed using the differential quadrature approach (DQA), which is an adaptation of the Dubner and Abate development for effectively inverting Laplace transforms. This mathematical framework provides insight for dynamic stability of CNT enhanced fibers in the textile industry and provide strategies for optimizing garment design. The model ultimately has potential implications of incorporating CNT reinforcement for developing high-performance fibers that perform well against external force and still have comfort and durability with clothing design.

Keywords: clothing design; higher-order shear deformation beam theory; differential quadrature approach; multi-scale hybrid nanocomposites; stability analysis

1. Introduction

Composite structures are increasingly becoming crucial in modern engineering due to their unique ability to combine the advantages of different materials, leading to improved performance, reduced weight, and enhanced durability (Analooei *et al*. 2023). In these structures, two or more distinct materials are combined at a microscopic or macroscopic level to form a new material with superior properties (Bagheri *et al*. 2024). The primary advantage of composite materials is their ability to offer strength and stiffness while minimizing weight, which is essential in industries like aerospace, automotive, and civil engineering (Ebrahimi *et al*. 2020). For example, in the aerospace industry, composite materials are used to reduce the weight of aircraft, resulting in fuel efficiency and improved performance (Forooghi *et al*. 2022). One of the most significant properties of composite materials is their flexibility in design, as engineers can tailor the composition and structure to meet specific mechanical, thermal, or electrical requirements (Bayat *et al*. 2024). This versatility enables engineers to optimize materials for demanding applications that require both strength and flexibility, such as in high-performance sports equipment or protective gear (Abdelmalek *et al*. 2019). Moreover, composite structures often exhibit higher resistance to corrosion, fatigue, and wear, making them ideal for long-term applications, including in marine environments and chemical industries (Adab *et al*. 2022). The growing use of composites also helps in energy conservation and sustainability. For instance, lighter and stronger composite materials contribute to lower energy consumption in transportation and building sectors (Afzali *et al*. 2023). In civil engineering, composites are used to reinforce or repair structures, extending their lifespan while minimizing the environmental impact of repairs (Ai and Gao 2017). The design flexibility of composite materials also allows for the development of complex geometries that would be difficult or impossible to achieve with traditional materials (Alsubaie *et al*. 2023). Furthermore, advances in nanotechnology and the incorporation of nanomaterials, such as carbon nanotubes or graphene, into composites have opened new frontiers in engineering (Adeniyi *et al*. 2023). These enhancements improve the mechanical properties at the nanoscale, resulting in composites with extraordinary strength-to-weight ratios and other performance benefits (Al-Osta 2022). As the demand for high-performance, cost-effective

*Corresponding author, Ph.D.,
E-mail: kuili01@email.cn

ISSN: 2287-237X (Print), 2287-2388 (Online)

materials continues to rise, composite structures will play an increasingly important role in engineering innovation, offering solutions to some of the most challenging problems faced by industries worldwide (Alijani and Amabili 2013).

Stability analysis is a fundamental aspect of structural engineering, as it ensures that a structure can withstand external forces without undergoing undesirable deformations or failures (Avcar *et al*. 2023). Engineers use stability analysis to predict how a structure will behave under various loading conditions, such as static, dynamic, and thermal loads (Ebrahimi *et al*. 2019). The importance of stability analysis lies in its ability to prevent catastrophic failures, which can have severe safety and financial consequences (Mangalasseri *et al*. 2023). For instance, the collapse of a bridge or building can result in loss of life, environmental damage, and costly repairs (Salari 2016). One of the primary goals of stability analysis is to determine the critical load at which a structure transitions from a stable state to an unstable one (Shen *et al*. 2024). This is particularly important for slender structures like columns, beams, and towers, which are prone to buckling under compressive loads (Abad and Rouzegar 2019). Stability analysis helps engineers identify the limits of a structure's performance, ensuring that it remains within safe operating conditions throughout its lifespan (Al-Furjan *et al*. 2022). In addition to static stability, engineers must also consider dynamic stability, especially for structures subjected to vibrations, wind loads, or seismic activity (Ayache *et al*. 2018). The dynamic response of a structure can lead to resonance phenomena, where small oscillations amplify and cause failure (Fallah *et al*. 2025). By analyzing the natural frequencies and damping characteristics of a structure, engineers can design systems that avoid resonance and enhance safety (Aminipour *et al*. 2018). For complex structures, such as bridges, skyscrapers, or aircraft, stability analysis also helps in optimizing material usage, ensuring that the design is both cost-effective and resilient (Niu and Yao 2021). With the advancement of computational methods, such as finite element analysis, engineers can now simulate and analyze the behavior of structures under various loading scenarios with high accuracy (Elangovan and Rajamohan 2022). Furthermore, stability analysis is crucial in the development of new materials and innovative construction techniques (Dashatan *et al*. 2023). For example, in the case of composite materials, engineers must assess how these new materials interact under load to ensure they maintain stability throughout their service life (Gordon *et al*. 2023). Understanding the stability of a structure also influences maintenance strategies, as engineers can predict when and where repairs are needed to prevent potential failures (Kazemi *et al*. 2025). Overall, stability analysis is vital for ensuring the safety, durability, and efficiency of structures, helping engineers create designs that can withstand the challenges of real-world conditions while minimizing risks to public safety (Rahimi *et al*. 2020).

A schematic view of the importance of the current work in clothing design is shown in Fig. 1.

Fig. 1 A schematic view of the importance of the current work in clothing design

This paper explores the stability and instability behavior of carbon nanotube-reinforced fibers in clothing design through advanced mathematical modeling. The textile thread is modeled as a double-clamped beam, representing the structural behavior under applied loads. The fibers are enhanced with multi-scale hybrid nanocomposites, incorporating CNTs to improve mechanical properties such as strength, stiffness, and resilience. The effective properties of the composite material are determined using the Halpin–Tsai model, which accounts for the reinforcing effects of CNTs on the matrix material. A quasi-3D hybrid type formulation based on higher-order shear deformation theory is employed to capture the fiber's deformation under external forces. This model accounts for both shear deformation and rotary inertia, which are crucial for accurately simulating the behavior of nanocomposite materials. The variational method is used to derive the governing equations of motion, and the system is subjected to a harmonically induced transverse force. Stability analysis is performed using the DQA, modified through the Dubner and Abate technique for efficient Laplace transform inversion. This study provides a comprehensive framework for understanding the dynamic behavior of CNT-enhanced fibers in clothing, offering valuable insights into their mechanical performance. The results can assist in optimizing the design of textile fibers for enhanced durability, flexibility, and comfort, contributing to the development of advanced materials in modern garment design.

2. Theory and formulation

2.1 Problem definition

Fig. 2 illustrates the expected beam's length, b breadth, and h thickness of the construction. The use of carbon-based reinforcements, namely CF and CNTs, must be mentioned.

2.2 Equivalent properties of multi-scale hybrid composites

This section describes the two-step homogenization method using a Halpin-Tsai model (Thostenson *et al*. 2002) which is integrated with a micromechanical approach (Shen 2009). CF-reinforced composites' effective properties will primarily be stated as (Ebrahimi and Habibi 2018):

$$E_{11} = V_{\mathrm{F}}E_{11}^{\mathrm{F}} + V_{\mathrm{NCM}}E^{\mathrm{NCM}} \tag{1a}$$

$$\frac{1}{G_{12}} = \frac{V_{\mathrm{F}}}{G_{12}^{\mathrm{F}}} + \frac{V_{\mathrm{NCM}}}{G^{\mathrm{NCM}}} \tag{1b}$$

$$\rho = V_{\mathrm{F}}\rho^{\mathrm{F}} + V_{\mathrm{NCM}}\rho^{\mathrm{NCM}} \tag{1c}$$

$$\nu_{12} = V_{\mathrm{F}}\nu^{\mathrm{F}} + V_{\mathrm{NCM}}\rho^{\mathrm{NCM}} \tag{1d}$$

where E, G, ν and ρ represent the mass density, Poisson's ratio, shear modulus, and Young's modulus, respectively. Clearly, fiber and nanocomposite matrix are indicated by the superscripts F and NCM, respectively. Additionally, V_{F} and V_{NCM} represent the volume fractions of the fiber and nanocomposite matrix, respectively. It is evident that these volume fractions are connected by (Ebrahimi and Habibi 2018):

$$V_{\mathrm{F}} + V_{\mathrm{NCM}} = 1. \tag{2}$$

The material characteristics of the nanocomposite matrix can now be shown in the following way (Ebrahimi and Habibi 2018) by expanding the Halpin–Tsai model:

$$E^{\mathrm{NCM}} = E^{\mathrm{M}}\left(\frac{5}{8}\left(\frac{1+2\beta_{\mathrm{dd}}V_{\mathrm{CNT}}}{1-\beta_{\mathrm{dd}}V_{\mathrm{CNT}}}\right) + \frac{3}{8}\left(\frac{1+2(l^{\mathrm{CNT}}/d^{\mathrm{CNT}})\beta_{\mathrm{dl}}V_{\mathrm{CNT}}}{1-\beta_{\mathrm{dl}}V_{\mathrm{CNT}}}\right)\right) \tag{3a}$$

$$\beta_{\mathrm{dl}} = \frac{(E_{11}^{\mathrm{CNT}}/E^{\mathrm{M}}) - (d^{\mathrm{CNT}}/4t^{\mathrm{CNT}})}{(E_{11}^{\mathrm{CNT}}/E^{\mathrm{M}}) + (l^{\mathrm{CNT}}/2t^{\mathrm{CNT}})} \tag{3b}$$

$$\beta_{\mathrm{dd}} = \frac{(E_{11}^{\mathrm{CNT}}/E^{\mathrm{M}}) - (d^{\mathrm{CNT}}/4t^{\mathrm{CNT}})}{(E_{11}^{\mathrm{CNT}}/E^{\mathrm{M}}) + (d^{\mathrm{CNT}}/2t^{\mathrm{CNT}})} \tag{3c}$$

where E^{CNT}, V_{CNT}, t^{CNT}, l^{CNT} and d^{CNT} stand for the length, thickness, volume fraction, Young's modulus, and outer diameter of CNT, respectively. Additionally, V_{M} and E^{M} account for the matrix's volume fraction and Young's modulus, respectively. The following formula can be used to get the volume fraction of CNT:

$$V_{\mathrm{CNT}} = \frac{W_{\mathrm{CNT}}}{W_{\mathrm{CNT}} + \left(\frac{\rho^{\mathrm{CNT}}}{\rho^{\mathrm{M}}}\right)(1-W_{\mathrm{CNT}})} \tag{4}$$

where ρ^{M} and ρ^{CNT} represent the mass densities of the matrix and CNT, respectively, and W_{CNT} represents the weight fraction of CNT. It is important to note that the volume percentages of matrix and CNT can be connected as follows:

$$V_{\mathrm{CNT}} + V_{\mathrm{M}} = 1 \tag{5}$$

In the end, the composite's equivalent mass density, Poisson's ratio, and shear modulus can be described as follows (Ebrahimi and Habibi 2018):

$$\rho^{\mathrm{NCM}} = V_{\mathrm{CNT}}\rho^{\mathrm{CNT}} + V_{\mathrm{M}}\rho^{\mathrm{M}}, \tag{6a}$$

$$\nu^{\mathrm{NCM}} = \nu^{\mathrm{M}}, \tag{6b}$$

$$G^{\mathrm{NCM}} = \frac{E^{\mathrm{NCM}}}{2(1+\nu^{\mathrm{NCM}})}. \tag{6c}$$

The geometrical and material characteristics of constituent materials can be found in Ref (Karimiasl *et al*. 2019).

2.2.1 Displacement field

The structure's kinematic fields, as determined by higher-order shear deformation theory (HSDT) of the quasi-3D hybrid type (q-3DHT), are (Tu *et al*. 2019)

$$\begin{aligned} u(X,Z,t) &= Z\left(\beta\frac{\partial w_b}{\partial X}(X,t) + \alpha\frac{\partial\theta}{\partial X}(X,t) - \frac{\partial w_s}{\partial X}(X,t)\right) + u_0(X,t) + f(Z)\frac{\partial w_b}{\partial X}(X,t), \\ v(X,Z,t) &= 0, \\ w(X,Z,t) &= w_b(X,t) + w_s(X,t) + g(Z)\theta(X,t) \end{aligned} \tag{7}$$

where $f(Z) = Z\cosh\left(\frac{1}{2}\right) - h\sinh\left(\frac{Z}{h}\right)$, $g(Z) = \frac{\pi Z}{h}$, $\alpha = -g\left(\frac{h}{2}\right)$, and $\beta = -f'\left(\frac{h}{2}\right) - 1$.

Also, the strains can be introduced as

$$\begin{Bmatrix}\varepsilon_{XX}\\ \varepsilon_{ZZ}\\ \gamma_{XZ}\end{Bmatrix} = \begin{Bmatrix}\varepsilon_{XX}^{0}\\ \varepsilon_{ZZ}^{0}\\ \gamma_{XZ}^{0}\end{Bmatrix} + Z\begin{Bmatrix}k_{XX}^{0}\\ k_{ZZ}^{0}\\ k_{XZ}^{0}\end{Bmatrix} + f(Z)\begin{Bmatrix}\varepsilon_{XX}^{*}\\ \varepsilon_{ZZ}^{*}\\ \gamma_{XZ}^{*}\end{Bmatrix} + g(Z)\begin{Bmatrix}k_{XX}^{*}\\ k_{ZZ}^{*}\\ k_{XZ}^{*}\end{Bmatrix} + \gamma(Z)\begin{Bmatrix}\varepsilon_{XX}^{**}\\ \varepsilon_{ZZ}^{**}\\ \gamma_{XZ}^{**}\end{Bmatrix} + \Gamma(Z)\begin{Bmatrix}k_{XX}^{**}\\ k_{ZZ}^{**}\\ k_{XZ}^{**}\end{Bmatrix}, \tag{8}$$

where $\gamma(Z) = \frac{\partial f(Z)}{\partial Z}$, and $\Gamma(Z) = \frac{\partial g(Z)}{\partial Z}$ Also

$$\begin{Bmatrix}\varepsilon_{XX}^{0}\\ \varepsilon_{ZZ}^{0}\\ \gamma_{XZ}^{0}\end{Bmatrix} = \begin{Bmatrix}\frac{\partial u_0}{\partial X}\\ w_1\\ \beta\frac{\partial w_b}{\partial X} + \alpha\frac{\partial\theta}{\partial X} + \frac{\partial w_b}{\partial X}\end{Bmatrix}, \quad \begin{Bmatrix}k_{XX}^{0}\\ k_{ZZ}^{0}\\ k_{XZ}^{0}\end{Bmatrix} = \begin{Bmatrix}\beta\frac{\partial^2 w_b}{\partial X^2} + \alpha\frac{\partial^2\theta}{\partial X^2} - \frac{\partial^2 w_s}{\partial X^2}\\ 0\\ 0\end{Bmatrix}, \tag{9a}$$

$$\begin{Bmatrix}\varepsilon_{XX}^{*}\\ \varepsilon_{ZZ}^{*}\\ \gamma_{XZ}^{*}\end{Bmatrix} = \begin{Bmatrix}\frac{\partial^2 w_b}{\partial X^2}\\ 0\\ 0\end{Bmatrix}, \quad \begin{Bmatrix}k_{XX}^{*}\\ k_{ZZ}^{*}\\ k_{XZ}^{*}\end{Bmatrix} = \begin{Bmatrix}0\\ 0\\ \frac{\partial\theta}{\partial X}\end{Bmatrix}, \quad \begin{Bmatrix}\varepsilon_{XX}^{**}\\ \varepsilon_{ZZ}^{**}\\ \gamma_{XZ}^{**}\end{Bmatrix} = \begin{Bmatrix}0\\ 0\\ \frac{\partial w_b}{\partial X}\end{Bmatrix}, \quad \begin{Bmatrix}k_{XX}^{**}\\ k_{ZZ}^{**}\\ k_{XZ}^{**}\end{Bmatrix} = \begin{Bmatrix}0\\ \Gamma(Z)\\ 0\end{Bmatrix}. \tag{9b}$$

Based on the strains, the stress fields can be written

$$\begin{Bmatrix}\sigma_{XX}\\ \sigma_{ZZ}\\ \tau_{XZ}\end{Bmatrix}=\begin{bmatrix}Q_{11} & Q_{13} & 0\\ Q_{31} & Q_{33} & 0\\ 0 & 0 & Q_{55}\end{bmatrix}\begin{Bmatrix}\varepsilon_{XX}\\ \varepsilon_{ZZ}\\ \gamma_{XZ}\end{Bmatrix} \tag{10}$$

where

$$Q_{11}=\frac{E_{11}}{1-\nu_{12}\nu_{21}},\ Q_{12}=\frac{\nu_{12}E_{22}}{1-\nu_{12}\nu_{21}}, \tag{11a}$$

$$Q_{22}=\frac{E_{22}}{1-\nu_{12}\nu_{21}},\ Q_{55}=G_{12}. \tag{11b}$$

2.3 Hamilton's principle and governing equations

The formulations are obtained by applying the variational approach, which is expressed in the following equation:

$$\int_{t_1}^{t_2}(\delta\Pi_k-\delta\Pi_e-\delta\Pi_w)dt=0 \tag{12}$$

In addition to kinetic energy, which can be expressed as follows, strain is represented by Π_e and Π_k.

$$\delta\Pi_k=\int\rho\left[\frac{\partial U}{\partial t}\frac{\partial\delta U}{\partial t}+\frac{\partial V}{\partial t}\frac{\partial\delta V}{\partial t}+\frac{\partial W}{\partial t}\frac{\partial\delta W}{\partial t}\right]dV, \tag{13a}$$

$$\delta\Pi_e=\int\{\sigma_{XX}\delta\varepsilon_{XX}+\sigma_{ZZ}\delta\varepsilon_{ZZ}+\tau_{XZ}\delta\gamma_{XZ}\}dV, \tag{13b}$$

The change in work done under a harmonically induced transverse force when mechanical loads are applied to a beam can be explained as

$$\delta\Pi_w=\int_A F(t)\delta w_0 dA \tag{14}$$

where $F(t)=P_0 sin(\Omega_{ext}t)$. P_0, Ω_{ext} shows the intensity load and excitation frequency. By substitution of Eqs. (13a), (13b), and (14) into Eq. (12), the following formulations can be attained

$$\delta u_0:\ \frac{\partial N_{XX}}{\partial X}=I_0\frac{\partial^2 u_0}{\partial t^2}+I_1\beta\frac{\partial^3 w_b}{\partial X\partial t^2}+I_1\alpha\frac{\partial^3\theta}{\partial X\partial t^2}-I_1\frac{\partial^3 w_s}{\partial X\partial t^2}+\mathrm{K}_0\frac{\partial^3 w_b}{\partial X\partial t^2}, \tag{15a}$$

$$\delta w_b:\ -\beta\frac{\partial^2 M_{XXb}}{\partial X^2}-\frac{\partial^2 P_{XXb}}{\partial X^2}+\beta\frac{\partial N_{XZb}}{\partial X}+\frac{\partial M_{XZb}}{\partial X}+\frac{\partial N_{XZb}}{\partial X}-F(t)=-\beta\frac{\partial}{\partial X}\left(I_1\frac{\partial^2 u_0}{\partial t^2}\right)-\beta^2\frac{\partial}{\partial X}\left(I_1\frac{\partial^3 w_b}{\partial X\partial t^2}\right)-\alpha\frac{\partial}{\partial X}\left(I_1\frac{\partial^3\theta}{\partial X\partial t^2}\right)+\frac{\partial}{\partial X}\left(I_1\frac{\partial^3 w_s}{\partial X\partial t^2}\right)-\frac{\partial}{\partial X}\left(K_2\frac{\partial^3 w_b}{\partial X\partial t^2}\right)-\beta\frac{\partial}{\partial X}\left(K_0\frac{\partial^2 u_0}{\partial t^2}\right)-\beta^2\frac{\partial}{\partial X}\left(K_2\frac{\partial^3 w_b}{\partial X\partial t^2}\right)-\alpha\frac{\partial}{\partial X}\left(K_2\frac{\partial^3\theta}{\partial X\partial t^2}\right)+\frac{\partial}{\partial X}\left(K_2\frac{\partial^3 w_s}{\partial X\partial t^2}\right)-\frac{\partial}{\partial X}\left(K_1\frac{\partial^3 w_b}{\partial X\partial t^2}\right)+\mathrm{I}_0\frac{\partial^2 w_b}{\partial t^2}+\mathrm{I}_0\frac{\partial^2 w_s}{\partial t^2}+\mathrm{K}_3\frac{\partial^2\theta}{\partial t^2}, \tag{15b}$$

$$\delta w_s:\ \frac{\partial^2 M_{XXb}}{\partial X^2}-F(t)=\frac{\partial}{\partial X}\left(I_1\frac{\partial^2 u_0}{\partial t^2}\right)+\beta\frac{\partial}{\partial X}\left(I_1\frac{\partial^3 w_b}{\partial X\partial t^2}\right)+\alpha\frac{\partial}{\partial X}\left(I_1\frac{\partial^3\theta}{\partial X\partial t^2}\right)-\frac{\partial}{\partial X}\left(I_1\frac{\partial^3 w_s}{\partial X\partial t^2}\right)+\frac{\partial}{\partial X}\left(K_2\frac{\partial^3 w_b}{\partial X\partial t^2}\right)+\mathrm{I}_0\frac{\partial^2 w_b}{\partial t^2}+\mathrm{I}_0\frac{\partial^2 w_s}{\partial t^2}+\mathrm{K}_3\frac{\partial^2\theta}{\partial t^2}, \tag{15c}$$

$$\delta\theta:\ -\alpha\frac{\partial^2 M_{XX}}{\partial X^2}-N_{ZZ}+\alpha\frac{\partial N_{XZ}}{\partial X}+\frac{\partial P_{XZ}}{\partial X}-F(t)\times g\left(\frac{h}{2}\right)=-\alpha\frac{\partial}{\partial X}\left(I_1\frac{\partial^2 u_0}{\partial t^2}\right)-\alpha\beta\frac{\partial}{\partial X}\left(I_2\frac{\partial^3 w_b}{\partial X\partial t^2}\right)-\alpha^2\frac{\partial}{\partial X}\left(I_2\frac{\partial^3\theta}{\partial X\partial t^2}\right)+\alpha\frac{\partial}{\partial X}\left(I_2\frac{\partial^3 w_s}{\partial X\partial t^2}\right)-\alpha\frac{\partial}{\partial X}\left(K_2\frac{\partial^3 w_b}{\partial X\partial t^2}\right)+\mathrm{K}_3\frac{\partial^2 w_b}{\partial t^2}+\mathrm{K}_3\frac{\partial^2 w_s}{\partial t^2}+\mathrm{K}_4\frac{\partial^2\theta}{\partial t^2}, \tag{15d}$$

where

$$\{I_0,I_1,I_2,K_0,K_1,K_2,K_3,K_4\}=\int_{-\frac{h}{2}}^{\frac{h}{2}}\int_0^L\begin{Bmatrix}1,Z,Z^2,f(Z),(f(Z))^2,\\ Zf(Z),g(Z),(g(Z))^2\end{Bmatrix}\rho dXdZ.$$

Additionally, the boundary conditions are as follows:

$$\delta u_0=0\quad or\quad N_{XX}\hat{n}_X=0, \tag{16a}$$

$$\delta w_b=0\quad or\quad \left(-\beta\frac{\partial M_{XX}}{\partial X}-\frac{\partial P_{XX}}{\partial X}+\beta N_{XZ}+N_{XZ}\right)\hat{n}_X=0, \tag{16b}$$

$$\delta w_s=0\quad or\quad \frac{\partial M_{XX}}{\partial X}\hat{n}_X=0, \tag{16c}$$

$$\delta\theta=0\quad or\quad \left(-\frac{\partial M_{XX}}{\partial X}+\alpha N_{XZ}+P_{XZ}\right)\hat{n}_X=0, \tag{16d}$$

$$\frac{\partial\delta w_b}{\partial X}=0\quad or\quad (\beta M_{XX}+P_{XX})n_X=0, \tag{16e}$$

$$\frac{\partial\delta w_s}{\partial X}=0\quad or\quad (M_{XX})n_X=0, \tag{16f}$$

$$\frac{\partial\delta\theta}{\partial X}=0\quad or\quad (\alpha M_{XX})n_X=0. \tag{16g}$$

where

$$N_{XXb}=\int_{-\frac{h}{2}}^{\frac{h}{2}}\int_0^L\sigma_{XX}\,dXdZ,\quad M_{XXb}=\int_{-\frac{h}{2}}^{\frac{h}{2}}\int_0^L Z\sigma_{XX}\,dXdZ,$$

$$N_{XX}=\int_{-\frac{h}{2}}^{\frac{h}{2}}\int_0^L\sigma_{XX}\,dXdZ,\ M_{XX}=\int_{-\frac{h}{2}}^{\frac{h}{2}}\int_0^L Z\sigma_{XX}\,dXdZ,$$

$$N_{XXs}=\int_{-\frac{h}{2}}^{\frac{h}{2}}\int_0^L\sigma_{XX}\,dXdZ,\ M_{XXs}=\int_{-\frac{h}{2}}^{\frac{h}{2}}\int_0^L Z\sigma_{XX}\,dXdZ,$$

$$P_{XXs}=\int_{-\frac{h}{2}}^{\frac{h}{2}}\int_0^L F(Z)\sigma_{XX}\,dZ,\quad N_{ZZs}=\int_{-\frac{h}{2}}^{\frac{h}{2}}\int_0^L \Gamma(Z)\sigma_{ZZ}\,dZ,$$

$$P_{XXb}=\int_{-\frac{h}{2}}^{\frac{h}{2}}\int_0^L F(Z)\sigma_{XX}\,dZ,\quad N_{ZZb}=\int_{-\frac{h}{2}}^{\frac{h}{2}}\int_0^L \Gamma(Z)\sigma_{ZZ}\,dZ, \tag{17}$$

$$P_{\mathcal{X}\mathcal{X}} = \int_{-\frac{h}{2}}^{\frac{h}{2}} \int_0^L F(\mathcal{Z})\sigma_{\mathcal{X}\mathcal{X}}\, d\mathcal{Z}, \quad N_{\mathcal{Z}\mathcal{Z}} = \int_{-\frac{h}{2}}^{\frac{h}{2}} \int_0^L \Gamma(\mathcal{Z})\sigma_{\mathcal{Z}\mathcal{Z}}\, d\mathcal{Z},$$

$$N_{\mathcal{X}\mathcal{Z}s} = \int_{-\frac{h}{2}}^{\frac{h}{2}} \int_0^L \tau_{\mathcal{X}\mathcal{Z}}\, d\mathcal{X}d\mathcal{Z}, \quad M_{\mathcal{X}\mathcal{Z}s} = \int_{-\frac{h}{2}}^{\frac{h}{2}} \int_0^L \gamma(\mathcal{Z})\tau_{\mathcal{X}\mathcal{Z}}\, d\mathcal{X}d\mathcal{Z},$$

$$P_{\mathcal{X}\mathcal{Z}s} = \int_{-\frac{h}{2}}^{\frac{h}{2}} \int_0^L g(\mathcal{Z})\tau_{\mathcal{X}\mathcal{Z}}\, d\mathcal{X}d\mathcal{Z}, \; N_{\mathcal{X}\mathcal{Z}b} = \int_{-\frac{h}{2}}^{\frac{h}{2}} \int_0^L \tau_{\mathcal{X}\mathcal{Z}}\, d\mathcal{X}d\mathcal{Z},$$

$$M_{\mathcal{X}\mathcal{Z}b} = \int_{-\frac{h}{2}}^{\frac{h}{2}} \int_0^L \gamma(\mathcal{Z})\tau_{\mathcal{X}\mathcal{Z}}\, d\mathcal{X}d\mathcal{Z}, \quad P_{\mathcal{X}\mathcal{Z}b} = \int_{-\frac{h}{2}}^{\frac{h}{2}} \int_0^L g(\mathcal{Z})\tau_{\mathcal{X}\mathcal{Z}}\, d\mathcal{X}d\mathcal{Z},$$

$$N_{\mathcal{X}\mathcal{Z}} = \int_{-\frac{h}{2}}^{\frac{h}{2}} \int_0^L \tau_{\mathcal{X}\mathcal{Z}}\, d\mathcal{X}d\mathcal{Z}, \quad M_{\mathcal{X}\mathcal{Z}} = \int_{-\frac{h}{2}}^{\frac{h}{2}} \int_0^L \gamma(\mathcal{Z})\tau_{\mathcal{X}\mathcal{Z}}\, d\mathcal{X}d\mathcal{Z}$$

$$P_{\mathcal{X}\mathcal{Z}} = \int_{-\frac{h}{2}}^{\frac{h}{2}} \int_0^L g(\mathcal{Z})\tau_{\mathcal{X}\mathcal{Z}}\, d\mathcal{X}d\mathcal{Z}.$$

3. Differential quadrature approach (DQA)

As a given one-dimensional function, the p^{th} derivative of $\mathcal{F}(\mathcal{X})$ would be defined as (Sun, Hao, Zhang, *et al*. 2024) using DQA.

$$\frac{\partial^p \mathcal{F}(\mathcal{X})}{\partial \mathcal{X}^p} = \sum_{j=1}^{\mathcal{N}_\mathcal{X}} \mathcal{A}_{ij}^{(p)} \mathcal{F}(\mathcal{X}_j) \; for \; i = 1,2,\ldots,\mathcal{N}_\mathcal{X} \tag{18}$$

Here, $\mathcal{N}_\mathcal{X}$ is the total number of grid-points, and $\mathcal{A}_{ij}^{(p)}$ denotes the weight coefficients for the i-th grid-point ($j = 1,2,\ldots,\mathcal{N}_\mathcal{X}$). Eq. (18) allows us to obtain $\mathcal{A}_{ij}^{(p)}$ for $i \neq j$ as follows:

$$\mathcal{A}_{ij}^{(p)} = p\left(\mathcal{A}_{ii}^{(p-1)}\mathcal{A}_{ij}^{(1)} - \frac{\mathcal{A}_{ij}^{(p-1)}}{\mathcal{X}_i - \mathcal{X}_j}\right), \quad p = 2,3,\ldots,\mathcal{N}_\mathcal{X} - 1 and \; i,j = 1,2,\ldots,\mathcal{N}_\mathcal{X} \tag{19}$$

Here, the following equation can be used to obtain $\mathcal{A}_{ij}^{(1)}$.

$$\mathcal{A}_{ij}^{(1)} = \frac{\mathcal{M}^{(1)}(\mathcal{X}_i)}{(\mathcal{X}_i - \mathcal{X}_j)\mathcal{M}^{(1)}(\mathcal{X}_j)}, i,j = 1,2,\ldots,\mathcal{N}_\mathcal{X} \tag{20}$$

The following formula would be used to ascertain $\mathcal{A}_{ij}^{(p)}$

$$\mathcal{A}_{ii}^{(p)} = -\sum_{j=1,j\neq i}^{\mathcal{N}} \mathcal{A}_{ij}^{(p)}, \quad i = 2,3,\ldots,\mathcal{N}_\mathcal{X} \; and \; p = 1,2,\ldots,\mathcal{N}_\mathcal{X} - 1 \tag{21}$$

$\mathcal{M}^{(1)}$ in Eq. (20) can be derived as

$$\mathcal{M}^{(1)}(\mathcal{X}_k) = -\sum_{j=1,j\neq k}^{\mathcal{N}_\mathcal{X}} (\mathcal{X}_k - \mathcal{X}_j), for \; k = 1,2,3,\ldots,\mathcal{N}_\mathcal{X} \tag{22}$$

with the Chebyshev–Gauss–Lobatto function, the grid-points ($\mathcal{X}_i$) can be coordinated as follows (Tornabene *et al*. 2015).

$$\mathcal{X}_i = \frac{L}{2}\left(1 - cos\left(\frac{(i-1)}{(\mathcal{N}_\mathcal{X} - 1)}\pi\right)\right) i = 1,2,3,\ldots,\mathcal{N}_\mathcal{X} \tag{23}$$

Therefore, by replacing Eqs. (17) and (18) with their corresponding values in Eq. (15a-d), we obtain the following equation:

$$[\mathbb{M}]\{\ddot{\mathbb{X}}(t)\} + [\mathbb{K}]\{\mathbb{X}(\boldsymbol{t})\} = \{\mathbf{F}(\mathbf{t})\}. \tag{24a}$$

$$\mathbb{X}(\boldsymbol{t}) = \{u_0 \;\; w_b \;\; w_s \;\; \theta\}^T. \tag{24b}$$

Using the following initial parameters chosen:

$$u_0(0) = 0, \; w_b(0) = 0, \; w_s(0) = 0, \; \theta(0) = 0, \quad \dot{u}_0(0) = 0, \; \dot{w}_b(0) = 0, \; \dot{w}_s(0) = 0, \; \dot{\theta}(0) = 0. \tag{25}$$

Applying the Laplace transform (Nguyen *et al*. 2022) to Eq. (24a) yields the following relations.

$$[\mathbb{M}]\{S^2 \times \hat{\mathbb{X}}(S)\} + [\mathbb{K}]\{\mathbb{X}(S)\} = \{\hat{\mathbb{F}}(\mathbf{S})\}, \tag{26a}$$

$$\hat{\mathbb{X}}(S) = \{\hat{u}_0 \;\; \hat{w}_b \;\; \hat{w}_s \;\; \hat{\theta}\}^T. \tag{26b}$$

$$\hat{\mathbb{F}}(S) = \left\{0 \;\; \hat{\mathrm{F}} \;\; \hat{\mathrm{F}} \;\; \hat{\mathrm{F}} \times \; g\left(\frac{h}{2}\right)\right\}^T. \tag{26c}$$

The layer-wise technique and the Laplace transform (Nguyen *et al*. 2022) can be used to determine the displacement for each layer after Eq. (26a) has been solved. The Laplace transform inversion is used to derive the displacements and stresses with time using the modified formulation of Dubner and Abate (Durbin 1974).

4. Results and discussion

4.1 Validation

Table 1 compares the first natural frequencies of CNT-reinforced composite beams under different values of the CNT volume fraction. The study compares results from a reference (Yas and Samadi 2012) and the present analysis. The table is structured into three columns: the CNT volume fraction, the reference values (Yas and Samadi 2012), and the corresponding first natural frequencies obtained in the current study. Three different V_{CNT} values are considered: 0.12, 0.17, and 0.28. For each of these values, the fundamental natural frequencies for CNT-reinforced beams are given. For example, when V_{CNT} is 0.12, the reference study reports a first natural frequency of 0.9753, whereas the present study's result is slightly lower at 0.9671. Similarly, for V_{CNT}= 0.17, the reference frequency is 1.1999, and the present result is marginally reduced at

Table 1 Comparison of the fundamental natural frequencies of CNTR nanocomposite beams (L/h = 15)

V_{CNT}		1st natural frequency
0.12	Ref. (Yas and Samadi 2012)	0.9753
	Present	0.9671
0.17	Ref. (Yas and Samadi 2012)	1.1999
	Present	1.1987
0.28	Ref. (Yas and Samadi 2012)	1.4401
	Present	1.4390

1.1987. Finally, for V_{CNT}= 0.28, the reference frequency is 1.4401, while the present frequency shows a slight increase to 1.4390. This comparison highlights the differences between the established model and the new model used in the present study. The discrepancies in the first natural frequencies between the reference and the present study may stem from the different modeling approaches, such as the use of higher-order shear deformation theory and a quasi-3D hybrid formulation in the present study. This table serves as an important benchmark to assess the accuracy and reliability of the new model for CNT-enhanced fiber materials in textile design.

4.2 Parametric results

Fig. 3a illustrates the transverse displacement response of the CNT-reinforced textile fiber, modeled as a double-clamped beam, subjected to harmonic excitation. The vertical axis represents the displacement www in meters, while the horizontal axis denotes time in seconds. Three curves are presented, each corresponding to a different CNT weight fraction. The data reveals that the inclusion of CNTs significantly influences the amplitude and frequency of the oscillations. Specifically, fibers with a lower CNT fraction exhibit larger amplitude fluctuation, indicative of higher susceptibility to instability under dynamic loading. As the CNT fraction increases, the displacement amplitude decreases, demonstrating enhanced stiffness and resistance to vibrational deformation. This result aligns with the Halpin–Tsai prediction of improved effective modulus with CNT integration. The presence of CNTs reinforces the fiber matrix, leading to more stable oscillatory behavior and reduced risk of resonance-induced failure. Additionally, the displacement curves reveal nonlinear features, suggesting the role of higher-order shear deformation effects as captured by the quasi-3D hybrid type formulation. The observed multi-frequency response patterns indicate that shear deformation and rotational inertia are effectively accounted for in the governing equations, as derived from the variational method. Overall, this subplot highlights the stabilizing effect of CNT reinforcement, where higher weight fractions result in dampened oscillatory displacement and improved structural resilience. These findings underscore the potential of CNT-enhanced fibers for clothing applications requiring mechanical robustness under repetitive or harmonic loading conditions. Fig. 3b presents the phase portrait of displacement against transverse velocity, offering a graphical depiction of the dynamic stability of CNT-reinforced textile fibers. This representation highlights the system's oscillatory states under harmonic loading, with distinct trajectories corresponding to CNT weight fractions. The phase curves form closed, periodic loops, reflecting the nonlinear dynamic behavior governed by the quasi-3D hybrid type formulation. For the lowest CNT fraction, the

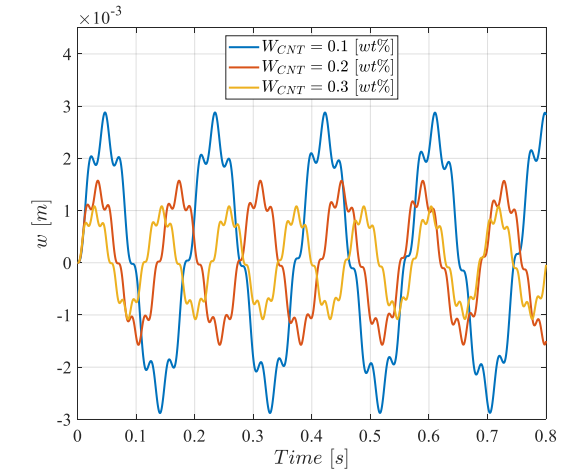

$a)\ w[m] - Time[s]$

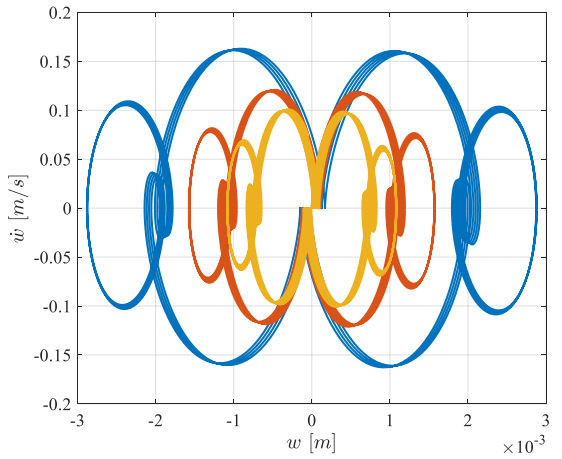

$b)\ w[m] - Time[s]$

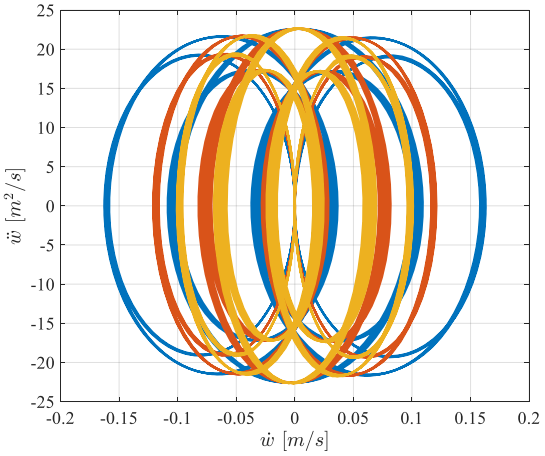

$c)\ \ddot{w}\left[\frac{m^2}{s}\right] - \dot{w}\left[\frac{m}{s}\right]$

Fig. 3 Three different plots that demonstrate the dynamic behavior of a system subjected to varying CNT weight fractions

trajectories are broader and more dispersed, indicating larger oscillation amplitudes and a reduced capacity for maintaining dynamic equilibrium. As the CNT fraction increases to 0.2% and 0.3%, the phase loops become more compact and symmetric, signifying improved energy dissipation and enhanced structural stability. This contraction of the phase space illustrates the stiffening effect predicted by the Halpin–Tsai model, where higher CNT content increases the effective modulus of the composite fiber. Furthermore, the closed-loop structures demonstrate the bounded nature of oscillations, consistent with the stability criteria derived from the Dubner–Abate modified differential quadrature approach. The system avoids divergence or chaotic response, suggesting that CNT reinforcement effectively mitigates instability phenomena. This phase space analysis provides deeper insight into the balance between kinetic and potential energy in CNT-enhanced fibers, revealing how weight fraction optimization directly influences vibrational resilience. From an application standpoint, these results imply that CNT-reinforced fibers maintain predictable and controlled dynamic responses, making them suitable for advanced textile engineering where stability under cyclic mechanical loads is critical. Fig. 3c illustrates the phase relationship between velocity and acceleration for CNT-reinforced fibers subjected to harmonic excitation. This velocity-acceleration phase portrait offers a higher-order perspective of the system's dynamic response, capturing the influence of CNT content on stability and energy transfer mechanisms. As in the previous subplots, three CNT weight fractions are compared. The trajectories exhibit closed, nested loops that reveal periodic but nonlinear oscillatory patterns. For the lowest CNT fraction, the trajectories extend outward, reflecting larger kinetic energy fluctuations and a reduced damping effect. This indicates higher instability potential and increased susceptibility to vibrational amplification. In contrast, the phase loops for 0.2% and 0.3% CNT weight fractions are more compact, symmetric, and confined, demonstrating greater stiffness, faster energy exchange cycles, and enhanced control of oscillatory motion. The dense clustering of trajectories suggests that CNT reinforcement minimizes the transfer of vibrational energy into instability modes. This behavior is consistent with the governing equations derived from the variational method and solved using the modified DQA, where CNT integration shifts the dynamic equilibrium towards stable limit cycles. Importantly, the phase structures confirm that acceleration responses remain bounded and predictable across CNT fractions, with higher reinforcement yielding smoother, more controlled oscillations. These findings emphasize that CNT-enhanced fibers possess superior resilience to dynamic instability, ensuring consistent performance under cyclic or harmonic loading. For clothing design applications, this translates into textiles that combine mechanical robustness with long-term durability, even under repetitive external excitations.

Fig. 4 presents three different plots that demonstrate the dynamic behavior of a system subjected to varying fiber volume fractions in the context of carbon nanotube-reinforced composite fibers. The analysis uses a mathematical model to assess how these fibers respond to external forces.

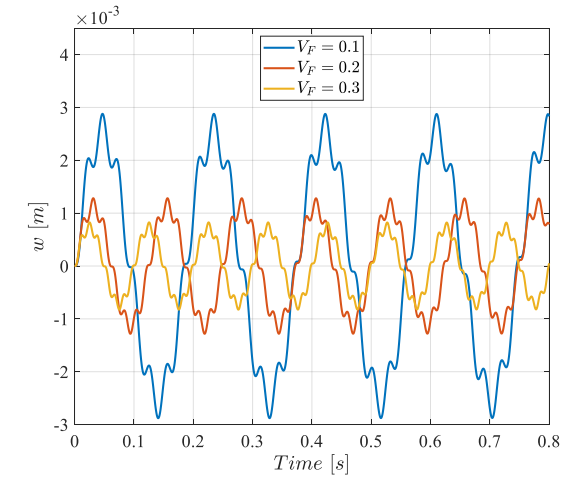

a) $w[m] - Time[s]$

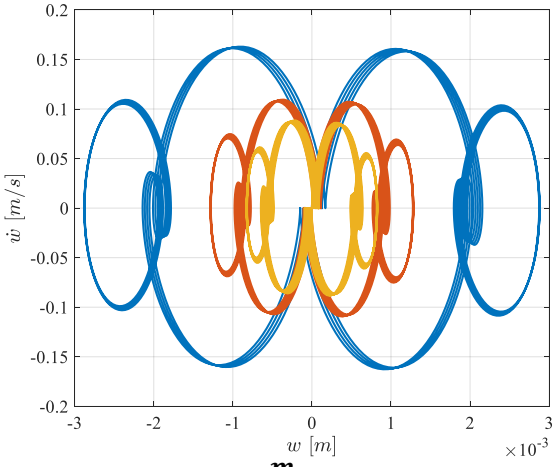

b) $\dot{w}\left[\frac{m}{s}\right] - w[m]$

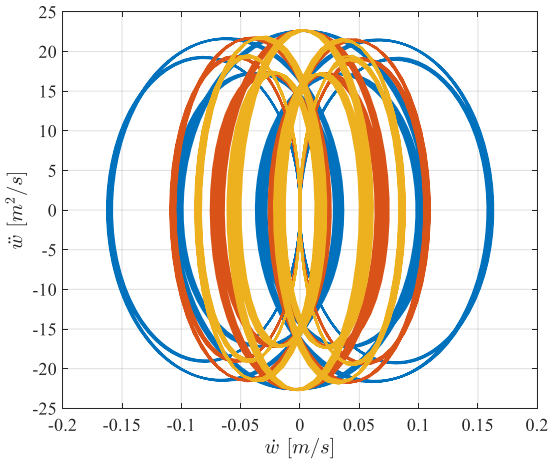

c) $\ddot{w}\left[\frac{m^2}{s}\right] - \dot{w}\left[\frac{m}{s}\right]$

Fig. 4 Three different plots that demonstrate the dynamic behavior of a system subjected to varying volume fraction of fibers

Each plot provides insight into the system's response at different stages of the analysis. Fig. 4a shows the time history of the displacement versus time for three distinct volume fractions of fiber. As expected, the displacement

increases with the volume fraction, with the highest displacement observed at $V_F = 0.3$, indicating greater flexibility or deformation of the fiber under dynamic loading conditions. The periodic oscillations reflect the natural oscillatory behavior of the system, with the frequency of oscillation appearing consistent across the different volume fractions. Fig. 4b represents the spatial distribution of the deflection across the beam length for different fiber volume fractions. This plot shows the shape of the beam's mode, with distinct patterns of deformation that change as the volume fraction increases. The curves for V_F = 0.1, 0.2, and 0.3 are distinctly separated, illustrating that as the fiber volume fraction increases, the beam undergoes more significant deformation, which impacts its overall stability. Fig. 4c shows a more detailed spatial deflection pattern, potentially reflecting higher-order modes of vibration. The differences in the deflection patterns suggest that the system's response becomes more complex as the CNT content in the fibers increases, indicating enhanced stiffness or different dynamic characteristics at higher V_F values. These results underline the importance of fiber volume fraction in tailoring the mechanical properties of CNT-reinforced composite fibers for specific applications, such as textile design and material optimization.

Fig. 5 illustrates the dynamic response of carbon nanotube-reinforced textile fibers modeled as a double-clamped beam under harmonically induced transverse excitation. The three subplots correspond to displacement, phase trajectory, and velocity–acceleration relations, enabling comprehensive insight into the system's stability characteristics. The top subplot depicts the transverse displacement as a function of time for varying excitation amplitudes. Increasing excitation amplitude results in higher oscillatory displacement, highlighting the nonlinear sensitivity of the system to external forcing. The middle subplot shows the phase portrait between displacement and velocity, where closed-loop trajectories emerge, representing periodic oscillatory states. Smaller excitation forces yield compact, symmetric loops, indicating stable bounded motion. As forcing magnitude increases, the loops broaden, signifying larger oscillation amplitudes and higher instability risk. The bottom subplot plots velocity against acceleration, extending the analysis to second-order dynamic behavior. Here, nested and circular patterns emerge, confirming periodicity while also revealing differences in stability margins under varying forcing amplitudes. Higher external forces lead to expanded trajectories, reflecting greater energy transfer and amplified instability tendencies. Collectively, the figure demonstrates the influence of harmonic forcing amplitude on fiber stability. The q-3DHT formulation effectively captures shear deformation and rotational inertia, while the Dubner–Abate modified differential quadrature approach ensures accurate solution convergence. These results emphasize the critical interplay between excitation magnitude and fiber stability, providing valuable insights for optimizing CNT-enhanced textile fibers in clothing applications requiring mechanical resilience.

Fig. 6 illustrates the influence of geometric slenderness ratio on the dynamic response of CNT-reinforced textile fibers subjected to harmonic excitation. The three subplots

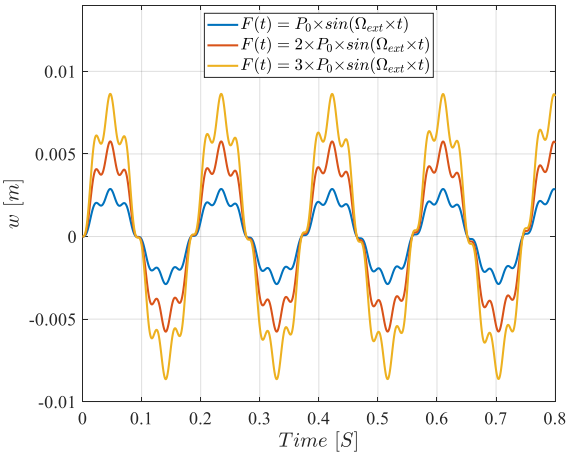

$$a)\ w[m] - Time[s]$$

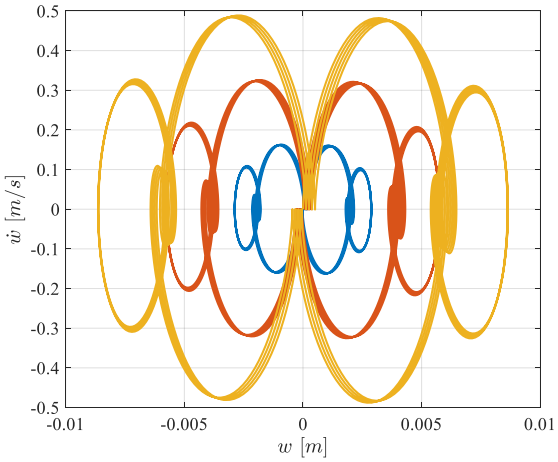

$$b)\ \dot{w}\left[\frac{m}{s}\right] - w[m]$$

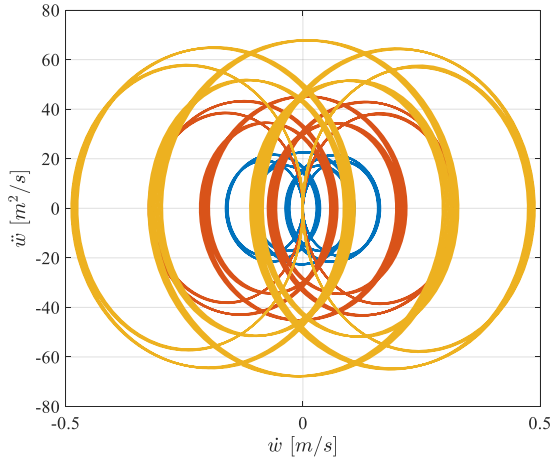

$$c)\ \ddot{w}\left[\frac{m^2}{s}\right] - \dot{w}\left[\frac{m}{s}\right]$$

Fig. 5 Three different plots that demonstrate the dynamic behavior of a system subjected to varying external excitations

collectively depict displacement evolution, phase trajectories, and velocity–acceleration relationships, providing insight into how variations in fiber geometry affect system stability. In the first subplot, the transverse displacement is plotted against time for slenderness ratios. The results show that

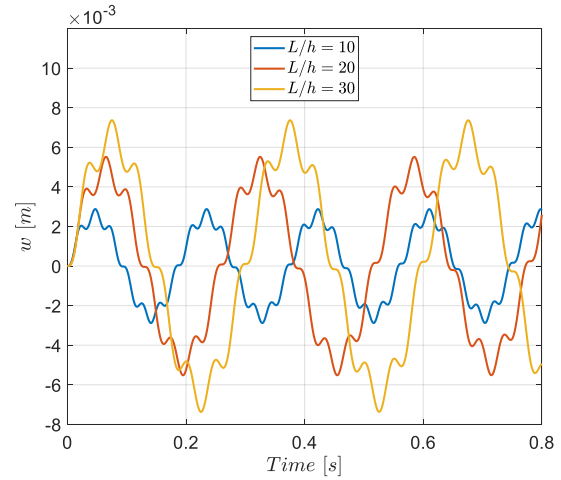

a) $w[m] - Time[s]$

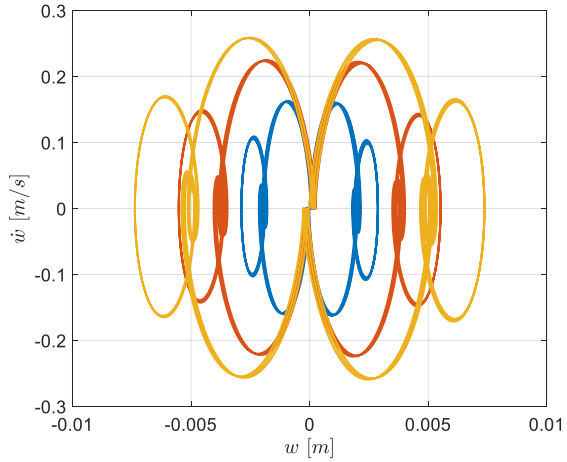

b) $\dot{w}\left[\frac{m}{s}\right] - w[m]$

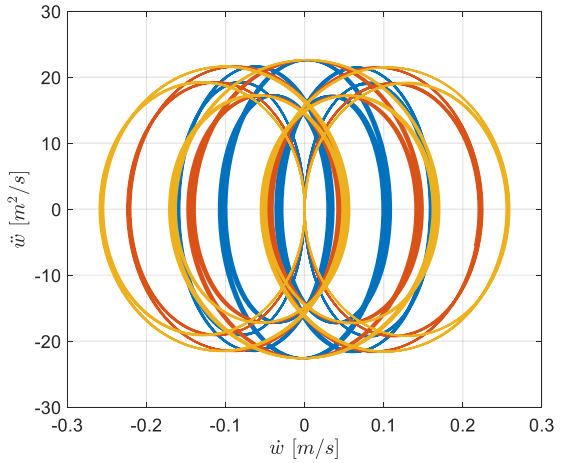

c) $\ddot{w}\left[\frac{m^2}{s}\right] - \dot{w}\left[\frac{m}{s}\right]$

Fig. 6 Three different plots that demonstrate the dynamic behavior of a system subjected to varying L/h rations

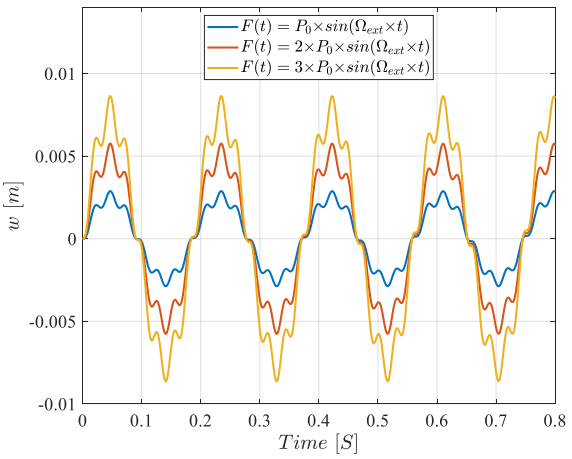

a) $w[m] - Time[s]$

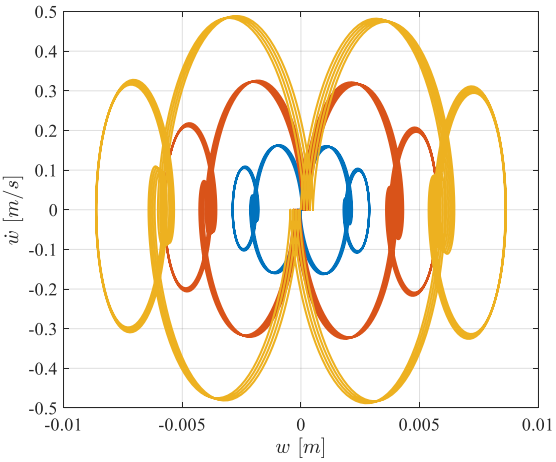

b) $\dot{w}\left[\frac{m}{s}\right] - w[m]$

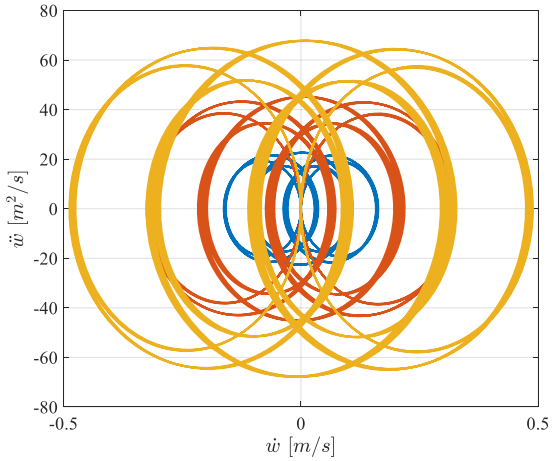

c) $\ddot{w}\left[\frac{m^2}{s}\right] - \dot{w}\left[\frac{m}{s}\right]$

Fig. 7 Three different plots that demonstrate the dynamic behavior of a system subjected to varying external excitation amplitude

increasing slenderness leads to larger displacement amplitudes, indicating higher susceptibility to vibrational deformation as beam flexibility increases. Shorter fibers demonstrate reduced amplitude oscillations, suggesting greater structural rigidity. The second subplot presents phase portraits of displacement versus velocity. The loops corresponding to higher slenderness ratios are broader and more dispersed, reflecting greater oscillation amplitudes and reduced dynamic stability. Conversely, compact loops at $L/h = 10$ indicate more controlled vibrational behavior.

This aligns with theoretical predictions that longer, thinner fibers possess lower stiffness and are more prone to dynamic instability. The third subplot illustrates velocity–acceleration phase space, highlighting second-order dynamic effects. Here, the trajectories expand outward with increasing slenderness, signifying higher kinetic and inertial responses. At $L/h = 30$, the phase loops are larger and more irregular, indicating amplified instability tendencies, while lower slenderness ratios produce bounded, symmetric patterns. Overall, the figure demonstrates that geometric slenderness plays a critical role in the vibrational stability of CNT-enhanced fibers, with higher L/h ratios reducing structural resilience. These findings underscore the importance of optimizing fiber geometry for textile applications requiring durability and dynamic stability.

Fig. 7a illustrates the transverse displacement of the CNT-enhanced fiber with respect to time. The x-axis represents the time in seconds, while the y-axis shows the displacement (in meters). Three curves are plotted, each corresponding to different excitation frequency amplitude. These curves represent the dynamic response of the fiber subjected to a harmonically induced transverse force, which is modeled as a sinusoidal function. As the excitation frequency increases, the amplitude of the oscillation also increases, indicating enhanced stiffness or reinforcement effect provided by the CNTs. The plot helps visualize how the fiber's behavior changes with varying excitation frequency. Fig. 7b represents the relationship between the velocity and the transverse displacement of the fiber. The plot shows multiple oscillations, with different regions marked by color codes corresponding to varying excitation frequency. This graph provides insight into the frequency-dependent behavior of the fiber, highlighting the shifts in resonant frequencies and stability characteristics when the excitation frequency is altered. The variation in these curves suggests that the excitation frequency influence the dynamic response and natural frequencies of the fiber. Fig. 7c is a phase space diagram, where the acceleration is plotted against the rate of change of transverse displacement. This graph is used to study the system's stability and dynamics in more detail. As seen from the plot, the system shows varying trajectories depending on the excitation frequency. The larger excitation frequency results in more stabilized oscillations, which is consistent with the increased rigidity and strength of the material. This diagram offers a deeper understanding of the system's stability across different conditions.

5. Conclusions

This study presented a comprehensive mathematical modeling approach to analyze the stability and instability of carbon nanotube-reinforced fibers used in clothing design. The model incorporated multi-scale hybrid nanocomposites, which significantly enhance the mechanical properties of the fibers, including their strength, flexibility, and durability. By modeling the textile thread as a double-clamped beam, the study was able to simulate the behavior of the fiber under external loads, with a particular focus on the stability of CNT-enhanced fibers. The use of a quasi-3D hybrid type formulation, based on higher-order shear deformation theory, allowed for a more accurate representation of the fiber's deformation, accounting for both shear deformation and rotary inertia. This is crucial when analyzing composite materials, as they exhibit complex behavior under load, including nonlinearities and interactions between the constituent materials. The application of the Halpin–Tsai model provided a means to characterize the effective properties of the hybrid nanocomposites, further refining the accuracy of the analysis. The stability analysis, conducted using the DQA and modified through the Dubner and Abate formulation for Laplace transform inversion, revealed critical insights into the behavior of CNT-reinforced fibers under harmonically induced transverse forces. This method, being both efficient and effective, enables the study of complex structural dynamics without the need for extensive computational resources. The results demonstrated that CNT reinforcement significantly improves the stability and mechanical properties of fibers, making them more suitable for high-performance textile applications. This mathematical framework offers valuable guidance for the design and optimization of CNT-enhanced fibers, facilitating the development of advanced garments with improved durability, comfort, and resilience. The findings from this study contribute to the growing body of research on nanocomposites and their applications in textile engineering, offering engineers a robust tool to predict the behavior of fiber-reinforced materials in real-world scenarios. Furthermore, the study underscores the importance of incorporating advanced modeling techniques to assess the stability of novel materials, ensuring the safety and performance of engineered structures in diverse applications. As the demand for high-performance fibers continues to rise, the integration of CNTs and advanced computational methods will play an increasingly pivotal role in revolutionizing the textile industry.

Acknowledgements

This project was funded by the China National Arts & Crafts Society under the 2024 research grant "Research on the Inheritance, Revitalization, and Innovation of Cao County Hanfu in the Context of Cultural Transformation and Urbanization" (Project No. CNACS2024-II-34).

References

Abad, F. and Rouzegar, J. (2019), "Exact wave propagation analysis of moderately thick levy-type plate with piezoelectric layers using spectral element method", *Thin Wall. Struct.*, **141**, 319-331. https://doi.org/10.1016/j.tws.2019.04.023

Abdelmalek, A., Bouazza, M., Zidour, M. and Benseddiq, N. (2019), "Hygrothermal effects on the free vibration behavior of composite plate using nth-order shear deformation theory: a micromechanical approach", *Iranian J. Sci. Technol. Transact. Mech. Eng.*, **43**, 61-73. https://doi.org/10.1007/s40997-018-0156-y

Adab, N., Arefi, M. and Amabili, M. (2022), "A comprehensive vibration analysis of rotating truncated sandwich conical

microshells including porous core and gpl-reinforced face-sheets", *Compos. Struct.*, **279**, 114761. https://doi.org/10.1016/j.compstruct.2022.114761

Adeniyi, A.G., Abdulkareem, S.A., Iwuozor, K.O., Abdulkareem, M.T., Adeyanju, C.A., Emenike, E.C., Ndagi, M. and Akande, O.J. (2023), "Mechanical and microstructural properties of expanded polyethylene powder/mica filled hybrid polystyrene composites", *Mech. Adv. Mater. Struct.*, **30**(13), 2610-2619. https://doi.org/10.1080/15376494.2021.1984476

Afzali, M., Farrokh, M. and Carrera, E. (2023), "Nonlinear thermal post-buckling analysis of rectangular FG plates using CUF", *Compos. Struct.*, **321**, 117282. https://doi.org/10.1016/j.compstruct.2023.117282

Ai, L. and Gao, X.L. (2017), "Metamaterials with negative poisson's ratio and non-positive thermal expansion", *Compos. Struct.*, **162**, 70-84. https://doi.org/10.1016/j.compstruct.2016.12.013

Al-Furjan, M., Xu, M., Farrokhian, A., Jafari, G.S., Shen, X. and Kolahchi, R. (2022), "On wave propagation in piezoelectric-auxetic honeycomb-2d-fgm micro-sandwich beams based on modified couple stress and refined zigzag theories", *Waves Random Complex Med.*, 1-25. https://doi.org/10.1080/17455030.2022.2092235

Alijani, F. and Amabili, M. (2013), "Nonlinear vibrations of laminated and sandwich rectangular plates with free edges. part 1: theory and numerical simulations", *Compos. Struct.*, **105**, 422-436. https://doi.org/10.1016/j.compstruct.2013.05.032

Al-Osta, M.A. (2022), "An exponential-trigonometric quasi-3d hsdt for wave propagation in an exponentially graded plate with microstructural defects", *Compos. Struct.*, **297**, 115984. https://doi.org/10.1016/j.compstruct.2022.115984

Alsubaie, A.M., Alfaqih, I., Al-Osta, M.A., Tounsi, A., Chikh, A., Mudhaffar, I.M. and Tahir, S. (2023), "Porosity-dependent vibration investigation of functionally graded carbon nanotube-reinforced composite beam", *Comput. Concr.*, **32**(1), 75-85. https://doi.org/10.12989/cac.2023.32.1.075

Aminipour, H., Janghorban, M. and Li, L. (2018), "A new model for wave propagation in functionally graded anisotropic doubly-curved shells", *Compos. Struct.*, **190**, 91-111. https://doi.org/10.1016/j.compstruct.2018.02.030

Analooei, H.R., Azhari, M. and Salehipour, H. (2023), "Thermo-electro-mechanical vibration and buckling analysis of quadrilateral and triangular nanoplates with the nonlocal finite strip method", *Mech. Based Des. Struct.*, **51**(3), 1684-1704. https://doi.org/10.1080/15397734.2021.1919902

Avcar, M., Hadji, L. and Civalek, O. (2023), "The influence of non-linear carbon nanotube reinforcement on the natural frequencies of composite beams", *Adv. Nano Res.*, **14**(5), 421-433. https://doi.org/10.12989/anr.2023.14.5.421

Ayache, B., Bennai, R., Fahsi, B., Fourn, H., Atmane, H.A. and Tounsi, A. (2018), "Analysis of wave propagation and free vibration of functionally graded porous material beam with a novel four variable refined theory", *Earthq. Struct.*, **15**(4), 369. https://doi.org/10.12989/eas.2018.15.4.369

Bagheri, H., Kiani, Y. and Eslami, M. (2024), "Application of gdq method to large amplitude response of fgm joined spherical-conical shells under rapid surface heating", *Mech. Based Des. Structu.*, **52**(5), 2869-2901. https://doi.org/10.1080/15397734.2022.2145490

Bayat, M.J., Kalhori, A., Babaei, M. and Asemi, K. (2024), "Natural frequency characteristics of stiffened fg multilayer graphene-reinforced composite plate with circular cutout resting on elastic foundation", *Int. J. Struct. Stabil. Dyn.*, **24**(18), 2450202. https://doi.org/10.1142/S0219455424502021

Dashatan, S.H., Parnas, L., Coker, D., Bozkurt, M.O. and Ozen, E.B. (2023), "In-situ observation and numerical study of dynamic delamination in tapered composite laminates", *Compos. Struct.*, **312**, 116841. https://doi.org/10.1016/j.compstruct.2023.116841

Durbin, F. (1974), "Numerical inversion of laplace transforms: An efficient improvement to Dubner and Abate's method", *Comput. J.*, **17**(4), 371-376. https://doi.org/10.1093/comjnl/17.4.371

Ebrahimi, F. and Habibi, S. (2018), "Nonlinear eccentric low-velocity impact response of a polymer-carbon nanotube-fiber multiscale nanocomposite plate resting on elastic foundations in hygrothermal environments", *Mech. Adv. Mater. Struct.*, **25**(5), 425-438. https://doi.org/10.1080/15376494.2017.1285453

Ebrahimi, F., Dehghan, M. and Seyfi, A. (2019), "Eringen's nonlocal elasticity theory for wave propagation analysis of magneto-electro-elastic nanotubes", *Adv. Nano Res.*, **7**(1), 1. https://doi.org/10.12989/anr.2019.7.1.001

Ebrahimi, F., Nouraei, M. and Dabbagh, A. (2020), "Modeling vibration behavior of embedded graphene-oxide powder-reinforced nanocomposite plates in thermal environment", *Mech. Based Des. Struct.*, **48**(2), 217-240. https://doi.org/10.1080/15397734.2019.1646138

Elangovan, H. and Rajamohan, V. (2022), "Dynamic characterization of tapered composite sandwich plate with honeycomb core: Numerical and experimental investigations", *Thin Walled Struct.*, **178**, 109515. https://doi.org/10.1016/j.tws.2022.109515

Fallah, F., Dehghanian, Z. and Farrahi, G. (2025), "Wave propagation characteristics in incompressible hyperelastic multi-layered cylindrical shells based on the shell theory", *Thin Walled Struct.*, 113191. https://doi.org/10.1016/j.tws.2025.113191

Forooghi, A., Fallahi, N., Alibeigloo, A., Forooghi, H. and Rezaey, S. (2022), "Static and thermal instability analysis of embedded functionally graded carbon nanotube-reinforced composite plates based on HSDT via GDQM and validated modeling by neural network", *Mech. Based Des. Struct.*, 1-34. https://doi.org/10.1080/15397734.2022.2104256

Gordon, T., Xu, X., Wisnom, M.R., Hallett, S.R. and Kim, B.C. (2023), "Improved impact damage resistance of tapered composite laminates using a ply scarfing technique", *Compos. Part A Appl. Sci. Manuf.*, **166**, 107391. https://doi.org/10.1016/j.compositesa.2022.107391

Karimiasl, M., Ebrahimi, F. and Akgöz, B. (2019), "Buckling and post-buckling responses of smart doubly curved composite shallow shells embedded in SMA fiber under hygro-thermal loading", *Compos. Struct.*, **223**, 110988. https://doi.org/10.1016/j.compstruct.2019.110988

Kazemi, E., Medeau, V., Greenhalgh, E., Pimenta, S., Finlayson, J. and Pinho, S.T. (2025), "A novel structural fuse concept for controlling failure path in tapered composite laminates", *Compos. Part A Appl. Sci. Manuf.*, **191**, 108714. https://doi.org/10.1016/j.compositesa.2024.108714

Mangalasseri, A.S., Mahesh, V., Mukunda, S., Mahesh, V., Ponnusami, S.A., Harursampath, D. and Tounsi, A. (2023), "Vibration based energy harvesting performance of magneto-electro-elastic beams reinforced with carbon nanotubes", *Adv. Nano Res.*, **14**(1), 27-43. https://doi.org/10.12989/anr.2023.14.1.027

Nguyen, S.N., Cho, M., Kim, J.S. and Han, J.W. (2022), "Improved thermo-mechanical-viscoelastic analysis of laminated composite structures via the enhanced lo-christensen-wu theory in the laplace domain", *Mech. Adv. Mater. Struct.*, 1-17. https://doi.org/10.1080/15376494.2022.2136301

Niu, Y. and Yao, M. (2021), "Linear and nonlinear vibrations of graphene platelet reinforced composite tapered plates and cylindrical panels", *Aerosp. Sci. Technol.*, **115**, 106798. https://doi.org/10.1016/j.ast.2021.106798

Rahimi, A., Alibeigloo, A. and Safarpour, M. (2020), "Three-

dimensional static and free vibration analysis of graphene platelet-reinforced porous composite cylindrical shell", *J. Vib. Control*, **26**(19-20), 1627-1645. https://doi.org/10.1177/1077546320916265

Salari, F.E.E. (2016), "Thermal loading effects on electro-mechanical vibration behavior of piezoelectrically actuated inhomogeneous size-dependent timoshenko nanobeams", *Adv. Nano Res.*, **4**(3), 197. https://doi.org/10.12989/anr.2016.4.3.197

Shen, H.S. (2009), "A comparison of buckling and postbuckling behavior of FGM plates with piezoelectric fiber reinforced composite actuators", *Compos. Struct.*, **91**(3), 375-384. https://doi.org/10.1016/j.compstruct.2009.06.007

Shen, X., Li, T., Xu, L., Kiarasi, F., Babaei, M. and Asemi, K. (2024), "Free vibration analysis of FG porous spherical cap reinforced by graphene platelet resting on winkler foundation", *Adv. Nano Res.*, **16**(1), 11-26. https://doi.org/10.12989/anr.2024.16.1.011

Sun, L., Hao, Y. X., Zhang, W. and Li, H. (2024), "Traveling wave vibration and critical rotating speed of rotating porous metal conical shell with elastic boundary conditions", *Aerosp. Sci. Technol.*, **148**, 109091. https://doi.org/10.1016/j.ast.2024.109091

Thostenson, E., Li, W., Wang, D., Ren, Z. and Chou, T. (2002), "Carbon nanotube/carbon fiber hybrid multiscale composites", *J. Appl. Phys.*, **91**(9), 6034-6037. https://doi.org/10.1063/1.1466880

Tornabene, F., Fantuzzi, N., Ubertini, F. and Viola, E. (2015), "Strong formulation finite element method based on differential quadrature: A survey", *Appl. Mech. Rev.*, **67**(2). https://doi.org/10.1115/1.4028859

Tu, T.M., Quoc, T.H. and Van Long, N. (2019), "Vibration analysis of functionally graded plates using the eight-unknown higher order shear deformation theory in thermal environments", *Aerosp. Sci. Technol.*, **84**, 698-711. https://doi.org/10.1016/j.ast.2018.11.021

Yas, M.H. and Samadi, N. (2012), "Free vibrations and buckling analysis of carbon nanotube-reinforced composite timoshenko beams on elastic foundation", *Int. J. Press. Vess. Piping*, **98**, 119-128. https://doi.org/10.1016/j.ijpvp.2012.07.012

CC